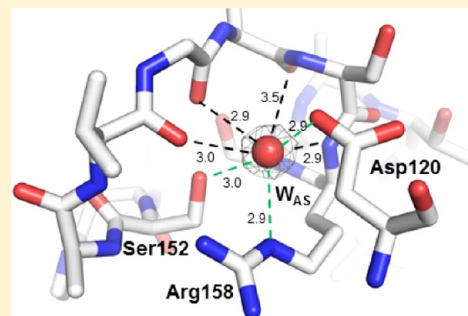


# Atomic Structure of Dual-Specificity Phosphatase 26, a Novel p53 Phosphatase

Ravi Kumar Lokareddy, Anshul Bhardwaj, and Gino Cingolani\*

Department of Biochemistry and Molecular Biology, Thomas Jefferson University, 233 South 10th Street, Philadelphia, Pennsylvania 19107, United States

**ABSTRACT:** Regulation of p53 phosphorylation is critical to control its stability and biological activity. Dual-specificity phosphatase 26 (DUSP26) is a brain phosphatase highly overexpressed in neuroblastoma, which has been implicated in dephosphorylating phospho-Ser20 and phospho-Ser37 in the p53 transactivation domain. In this paper, we report the 1.68 Å crystal structure of a catalytically inactive mutant (Cys152Ser) of DUSP26 lacking the first 60 N-terminal residues ( $\Delta$ N60-C/S-DUSP26). This structure reveals the architecture of a dual-specificity phosphatase domain related in structure to *Vaccinia* virus VH1. DUSP26 adopts a closed conformation of the protein tyrosine phosphatase (PTP)-binding loop, which results in an unusually shallow active site pocket and buried catalytic cysteine. A water molecule trapped inside the PTP-binding loop makes close contacts both with main chain and with side chain atoms. The hydrodynamic radius ( $R_H$ ) of  $\Delta$ N60-C/S-DUSP26 measured from velocity sedimentation analysis ( $R_H \sim 22.7$  Å) and gel filtration chromatography ( $R_H \sim 21.0$  Å) is consistent with an  $\sim 18$  kDa globular monomeric protein. Instead in crystal,  $\Delta$ N60-C/S-DUSP26 is more elongated ( $R_H \sim 37.9$  Å), likely because of the extended conformation of C-terminal helix  $\alpha_9$ , which swings away from the phosphatase core to generate a highly basic surface. As in the case of phosphatase MKP-4, we propose that a substrate-induced conformational change, possibly involving rearrangement of helix  $\alpha_9$  with respect to the phosphatase core, allows DUSP26 to adopt a catalytically active conformation. The structural characterization of DUSP26 presented in this paper provides the first atomic insight into this disease-associated phosphatase.



Dual-specificity phosphatases (DSPs) represent a heterogeneous subclass of the protein tyrosine phosphatase (PTP) superfamily characterized by the unique ability to dephosphorylate both phospho-tyrosine- and phospho-serine/threonine-containing substrates.<sup>1–5</sup> The first identified member of this family, VH1, is encoded by the *Vaccinia* virus H1 locus, which is conserved in all viruses of the Poxviridae family.<sup>6,7</sup> Since its identification in 1991, the number of VH1-like DSPs has quickly grown and, to date, includes 61 members divided into seven diverse subgroups.<sup>5</sup> The human genome encodes 38 different VH1-like DSPs<sup>5</sup> (also termed “DUSPs”<sup>5</sup>) that are essential cell signaling enzymes implicated in a multitude of physiological and pathological processes.<sup>5</sup> Similar to classical PTPs, DSPs contain a catalytic triad consisting of a Cys, an Arg, and an Asp.<sup>8</sup> Whereas the catalytic Cys and Arg are part of a phosphate-binding loop (or “PTP signature motif”) that has a consensus Cys(X)<sub>5</sub>Arg(Ser/Thr) sequence, the highly conserved Asp residue is located on a separate loop (known as the “general acid loop”), near the top of the active site, usually 30–40 residues from the active site motif in the primary sequence.<sup>8</sup> DSPs share a similar catalytic mechanism with PTPs, characterized by the formation of a transient enzyme–phospho-substrate intermediate.<sup>1,2</sup> Unlike PTPs, DSPs have broader substrate specificity<sup>9</sup> and can also dephosphorylate nonpeptidic substrates. Examples of DSPs specific to nonpeptidic substrates include PTEN-like DSPs that dephosphorylate D3-inositol phospholipids,<sup>10</sup> PIR that dephosphorylates mRNA,<sup>11</sup> and the glycogen

phosphatase laforin.<sup>12</sup> The high-resolution structure of *Vaccinia* virus VH1, determined to 1.32 Å resolution,<sup>13,14</sup> as well as a wealth of other DSP structures determined over the past 20 years,<sup>8</sup> has revealed that the DSP active site consists of a shallow, surface-exposed pocket, usually only  $\sim 6$  Å in depth. This active site is simple and likely not sufficient to discriminate among the thousands of different phospho-substrates present, at any given time, in a living cell.<sup>3</sup> Instead, substrate recognition and specificity are likely achieved by a dedicated tertiary/quaternary structural complementarity between the phosphatase and its target phospho-substrate.

DUSP26, also known as MKP-8 (mitogen-activated protein kinase phosphatase-8<sup>15</sup>), LDP-4 (low-molecular mass DUSP-4<sup>16</sup>), or SKRP3 (stress-activated protein kinase pathway-regulating phosphatase), is a human DSP of the VH1 superfamily. DUSP26 is mainly expressed in neurons,<sup>17</sup> retina,<sup>16,18</sup> heart,<sup>15,17</sup> adrenal gland,<sup>18</sup> and skeletal muscle,<sup>15,17,18</sup> where it localizes primarily to the cell nucleus.<sup>15,16</sup> Several potential substrates of DUSP26 have been identified. DUSP26 can function as a p38-specific phosphatase<sup>15,19</sup> and an Erk-phosphatase,<sup>17</sup> and in PC12 cells, overexpression of DUSP26 was found to downregulate the PI3K/Akt signaling pathway.<sup>18</sup> Furthermore, several direct and indirect lines of evidence

Received: October 30, 2012

Revised: December 21, 2012

Published: January 8, 2013



connect DUSP26 biology to tumorigenesis. First, DUSP26 inhibits p38-mediated apoptosis, thereby promoting anaplastic thyroid cancer cell growth and survival.<sup>19</sup> Second, DUSP26 associates with and dephosphorylates Kap3, a component of the microtubule-directed protein complex KIF3, supporting a role in intracellular transport of  $\beta$ -catenin/N-cadherin (an established KIF3 cargo) and cell–cell adhesion.<sup>20</sup> Finally, DUSP26 has been shown to directly bind to and dephosphorylate the p53 transactivation domain (TAD) at Ser20 and Ser37, which results in repression of p53 transcriptional activity.<sup>21</sup> DUSP26 expression is greatly unregulated in neuroblastoma cell lines, which, unlike many human cancer cells, maintain normal levels of wild-type p53. Overexpression of DUSP26 suppresses p53 “onco-suppressive” function in response to genotoxic stress.<sup>21</sup> For this reason, DUSP26 is a novel and promising target for the development of small molecule inhibitors for the treatment of neuroblastoma and related pediatric malignancies. In this paper, we report a structural and biochemical characterization of human DUSP26. This work sheds light on the organization of a p53 phosphatase whose hyperactivation is linked to neuroblastoma.

## ■ EXPERIMENTAL PROCEDURES

**Molecular Biology and Biochemical Techniques.** A synthetic gene encoding human DUSP26 was cloned in expression vector pET21b containing a C-terminal six-histidine (6x-His) tag between restriction sites *Nde*I and *Xho*I (FL-DUSP26). Constructs lacking N-terminal residues 1–14 ( $\Delta$ N14-DUSP26), 1–60 ( $\Delta$ N60-DUSP26), and a core fragment spanning residues 61–187 (DUSP26-core) were generated by long polymerase chain reaction using FL-DUSP26 as a template.  $\Delta$ N60-C/S-DUSP26 and C/S-DUSP26-core were generated by site-directed mutagenesis of Cys152 to Ser. All DUSP26 constructs were expressed in *Escherichia coli* strain BL21(DE3)-RIL for 9 h at 25 °C after induction with 0.4 mM IPTG at an OD<sub>600</sub> of ~0.5. FL- and  $\Delta$ N14-DUSP26 were completely insoluble, while constructs  $\Delta$ N60-DUSP26,  $\Delta$ N60-C/S-DUSP26, DUSP26-core, and C/S-DUSP26-core were recovered in the soluble fraction. Soluble DUSP26 constructs were purified by immobilized metal affinity chromatography using TALON metal affinity resin (Clontech) followed by gel filtration chromatography on a Superdex 75 column 16/60 (GE Healthcare Life Sciences) in 150 mM sodium chloride, 20 mM HEPES (pH 7.5), 5 mM  $\beta$ -mercaptoethanol, and 0.1 mM PMSF. Purified DUSP26 constructs were concentrated to ~3 mg/mL using a 10K molecular weight cutoff Vivaspin 15 concentrator (Sartorius). The Superdex 75 gel filtration column was calibrated using cytochrome *c* (12.4 kDa), carbonic anhydrase (29 kDa), albumin (66 kDa), alcohol dehydrogenase (150 kDa), and blue dextran (2000 kDa) from the Gel Filtration Molecular Weight Markers Kit (Sigma). The hydrodynamic radius ( $R_H$ ) of  $\Delta$ N60-C/S-DUSP26 was determined by gel filtration chromatography<sup>22</sup> knowing the hydrodynamic radii of protein standards:<sup>23</sup> cytochrome *c*, 17 Å; carbonic anhydrase, 23.6 Å; albumin, 35.5 Å; alcohol dehydrogenase, 45.5 Å.

**In Solution Biophysical Characterization.** Circular dichroism (CD) spectra were recorded using a Jasco J-810 spectropolarimeter equipped with a Peltier temperature control system. Samples were measured in a rectangular quartz cuvette with a path length of 1 cm at a final protein concentration of 10  $\mu$ M in 20 mM HEPES (pH 7.0) and 150 mM NaCl at 20 °C. Temperature-induced unfolding of DUSP26 was monitored by recording variations in ellipticity at 222 nm as a function of temperature in 1.0 °C increments from 20 to 80 °C,

as previously described.<sup>13,24</sup> The reversibility of unfolding was checked by slowly cooling unfolded DUSP26 to 20 °C followed by a second scan, which revealed DUSP26 unfolding is irreversible. The apparent melting temperatures ( $appT_m$ ) observed for  $\Delta$ N60-C/S-DUSP26 and catalytically active  $\Delta$ N60-DUSP26 were 69 and 68 °C, respectively, while for DUSP26-core,  $appT_m$  was 59 °C. To determine the oligomeric state of DUSP26 in solution, purified  $\Delta$ N60-DUSP26,  $\Delta$ N60-C/S-DUSP26, and C/S-DUSP26-core in 20 mM HEPES (pH 7.0) and 150 mM sodium chloride were analyzed in a Beckman Coulter ProteomeLab XL-1 analytical ultracentrifuge in velocity sedimentation mode; 400  $\mu$ L of sample and 420  $\mu$ L of reference buffer were loaded into separate compartments of a 12 mm path-length Epon centerpiece cell. Runs were performed at 40000 rpm and 20 °C. Absorbance values were collected at a wavelength of 278 nm using 5–100  $\mu$ M protein samples. The data were fit using a continuous sedimentation coefficient [ $c(s)$ ] distribution model, and an estimated molecular mass was obtained with SEDFIT [P. Schuck, National Institutes of Health, Bethesda, MD (<http://www.analyticalultracentrifugation.com/download.htm>)]. Both the CD spectropolarimeter and the analytical ultracentrifuge used in this study are part of the Kimmel Cancer Center X-ray Crystallography and Molecular Characterization shared resource facility, at Thomas Jefferson University.

**Crystallization, Data Collection, and Structure Determination.** Crystals of  $\Delta$ N60-C/S-DUSP26 were obtained using the hanging drop vapor diffusion methods by mixing together 2  $\mu$ L of gel filtration purified protein at 3 mg/mL with 1  $\mu$ L of 0.15 M calcium acetate hydrate, 0.1 M sodium cacodylate trihydrate (pH 6.5), and 17% (w/v) polyethylene glycol 8000, at 18 °C. Crystals appeared within a few hours and grew to a maximal length of ~150  $\mu$ m in 3 days.  $\Delta$ N60-C/S-DUSP26 crystals were harvested in nylon cryo-loops and using 30% glycerol as a cryoprotectant and flash-frozen in liquid nitrogen. Diffraction data were collected at beamlines X6A and X29 at the National Synchrotron Light Source (NSLS) on ADSC Quantum Q270 and Quantum-315r CCD detectors, respectively. Data indexing, integration, and scaling were conducted with HKL2000.<sup>25</sup> The asymmetric unit contains four copies of  $\Delta$ N60-C/S-DUSP26 arranged into two dimers (termed protomers A, B, C, and D) with ~42% solvent content. The structure of  $\Delta$ N60-C/S-DUSP26 was determined by molecular replacement using an ensemble search model containing the DSP-core of phosphatases VH1 [Protein Data Bank (PDB) entry 3CM3] and DUSP27 (PDB entry 2Y96), as implemented in PHASER.<sup>26</sup> This initial phasing model was subjected to rounds of manual rebuilding using COOT<sup>27</sup> followed by refinement with phenix.refine, from the PHENIX software suite,<sup>28</sup> and Refmac,<sup>29</sup> using cycles of positional and anisotropic *B* factor refinement, enforcing torsional noncrystallographic symmetry restraints. The final atomic model of  $\Delta$ N60-C/S-DUSP26 has  $R_{work}$  and  $R_{free}$  values of 18.5 and 21.5%, respectively, calculated using all diffraction data between 10 and 1.68 Å resolution (Table 2). The test set for the calculation of  $R_{free}$  was defined using 3540 randomly chosen reflections. The final atomic model of  $\Delta$ N60-C/S-DUSP26 contains residues 61–211 for protomers A–C and residues 61–209 for protomer D and 532 water molecules. All protomers contain an additional N-terminal methionine at position 60; at the C-terminus, protomers A and B contain two additional residues (Leu/Glu) and protomer C contains only one additional residue (Leu) from the cloning site. The stereochemistry was checked using PROCHECK:<sup>30</sup> the final model has good geometry with root-mean-square deviations (rmsds) from ideal bonds and angles of

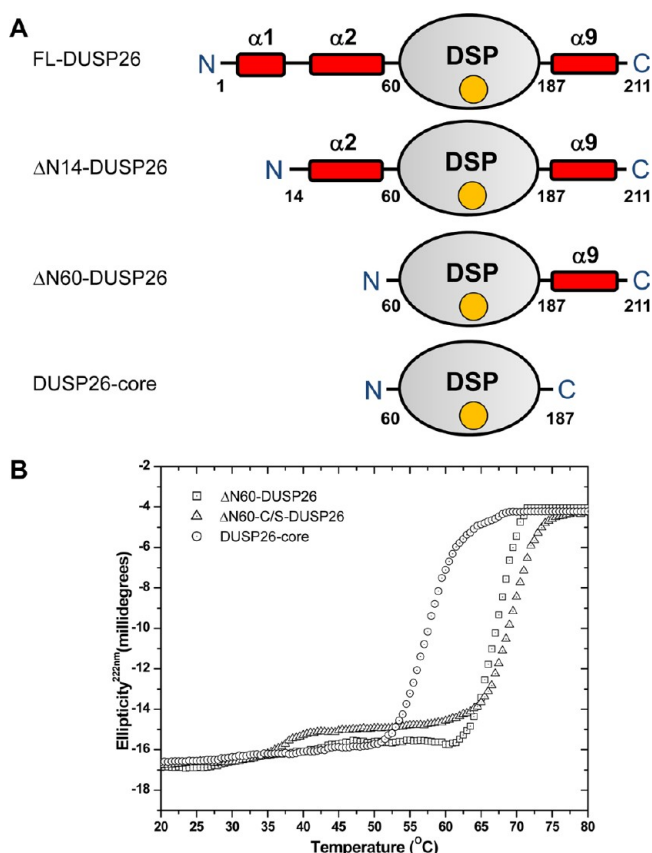


**Figure 1.** Domain organization and stability of DUSP26. (A) Schematic diagram of DUSP26 domain organization and deletion constructs generated in this study. The DSP domain (residues 61–186) is colored gray and is flanked by two predicted N-terminal  $\alpha$ -helices ( $\alpha 1$  and  $\alpha 2$ ) and a C-terminal helix ( $\alpha 9$ ) (colored red). (B) Stability of DUSP26 against thermal denaturation monitored by measuring changes in the ellipticity intensity at 222 nm as a function of temperature. The concentration of DUSP26 constructs used in this experiment was 10  $\mu$ M. All  $T_m$  values measured in this experiment were apparent ( $appT_m$ ) as DUSP26 constructs unfolded irreversibly. A complete list of  $appT_m$  values is given in Table 1.

0.006 Å and 1.0°, respectively. The Ramachandran plot shows 95.5% of residues in the most favored regions, 4.5% of residues in additional allowed regions, and no residues in disallowed residues. Refinement and data collection statistics are listed in Table 2.

**Structure Analysis.** All ribbon diagrams and surface representations in the paper were prepared using Pymol.<sup>31</sup> Nonlinear Poisson–Boltzmann electrostatic calculations were performed using APBS Tools.<sup>32</sup> The topological diagram was generated using PDBsum,<sup>33</sup> and structural superimpositions were conducted

in Coot.<sup>27</sup> The interface surface area was analyzed using the PISA server.<sup>34</sup> Hydrodynamic radii were calculated from atomic coordinates using HYDROPRO.<sup>35</sup> Atomic coordinates and experimental structure factors have been deposited as PDB entry 4HRF.

## RESULTS

### Domain Organization and Stability of DUSP26.

DUSP26 consists of 211 residues and has a predicted molecular mass of ~23945 Da. Bioinformatics analysis of DUSP26 organization reveals a central DSP-core spanning residues 61–186 surrounded by two predicted N-terminal  $\alpha$ -helices (helix  $\alpha 1$ , residues 5–14;  $\alpha 2$ , residues 40–58) and a C-terminal helix ( $\alpha 9$ , residues 187–211) (Figure 1A). Aiming at structural studies, we synthesized the gene encoding human DUSP26 and expressed it in bacteria fused to a C-terminal 6x-His tag. Attempts to purify full-length DUSP26 (FL-DUSP26) under native conditions, in the presence of nonionic detergents, or DUSP26 fused to a large affinity tag were unsuccessful, because of the marked insolubility of the phosphatase. As the first 60 residues of DUSP26 are highly enriched in hydrophobic amino acids, we generated two N-terminally deleted constructs lacking either helix  $\alpha 1$  ( $\Delta N14$ -DUSP26) or both helices  $\alpha 1$  and  $\alpha 2$  ( $\Delta N60$ -DUSP26), as well as a minimal DUSP26-core (residue 61–187) spanning only the predicted phosphatase core (Figure 1A). These constructs displayed different solubilities when expressed in bacteria, and among them, only  $\Delta N60$ -DUSP26 and to a lesser extent DUSP26-core could be purified under native conditions for biophysical analysis.

To assess the conformational stability of DUSP26 and determine how N- and C-terminal deletions destabilized the protein, we measured heat-induced denaturation by monitoring variations in ellipticity at 222 nm as a function of temperature (Figure 1B and Table 1).  $\Delta N60$ -DUSP26 was found to unfold irreversibly in a highly cooperative manner, with an apparent melting temperature ( $appT_m$ ) of ~68 °C. Replacing the active site cysteine 152 with serine yielded an inactive phosphatase ( $\Delta N60$ -C/S-DUSP26) that was less prone to aggregation in solution and of comparable thermal stability ( $appT_m$  ~ 69 °C). Instead, the smaller DUSP26-core had a significantly reduced thermal stability ( $appT_m$  ~ 59 °C), consistent with the lack of structural determinants at both N- and C-termini. Thus, DUSP26 is a stable protein phosphatase; N- and C-terminal structural elements flanking the predicted DSP-core affect the enzyme stability likely by mediating intra- or intermolecular interactions.

**$\Delta N60$ -DUSP26 Is Monomeric in Solution.** The DUSP26 oligomeric state was investigated in solution by AUC sedimentation velocity analysis. As FL-DUSP26 was completely insoluble, we restricted our analysis to  $\Delta N60$ -DUSP26 and DUSP26-core, which are soluble under physiological conditions. Figure 2A shows

**Table 1.** Biophysical Parameters Measured by CD, AUC, and Gel Filtration Chromatography for the Study of DUSP26 Conformational Stability and Oligomeric State

protein	$appT_m$ (°C)	apparent sedimentation coefficient, $s^a$ (S)	standardized sedimentation coefficient, $s_{20,w}$ (S)	frictional ratio ( $f/f_0$ )	hydrodynamic radius, $R_H$ (Å) <sup>a</sup>	calculated mass (kDa)	theoretical mass (kDa) <sup>b</sup>
$\Delta N60$ - DUSP26	68	1.925	2.012	1.23	22.7/21.0	18.1	18.2
$\Delta N60$ -C/S- DUSP26	69	1.922	2.007	1.23	22.7/21.0	18.1	18.2
DUSP26- CORE	59	1.811	1.948	1.20	20.2/20.0	16.6	15.4

<sup>a</sup>Hydrodynamic radius from AUC and gel filtration. <sup>b</sup>The theoretical mass includes additional C-terminal residues introduced by cloning (GLEALEHHHHHH).



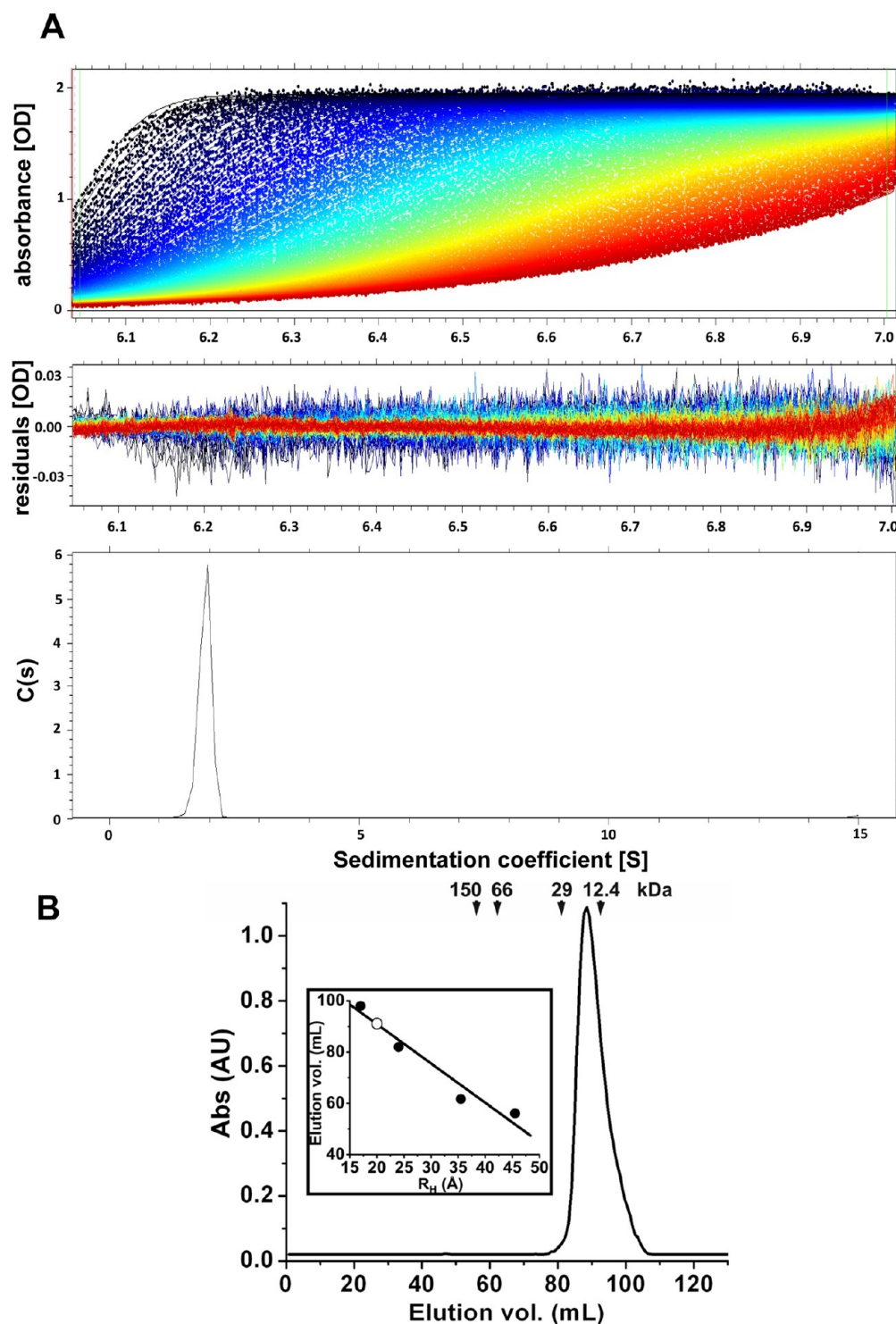


**Figure 2.** DUSP26 exists as a monomer in solution. (A) Sedimentation velocity profiles of  $\Delta N60\text{-C/S-DUSP26}$  measured in 0.15 M sodium chloride at 20 °C. The top panel shows the raw absorbance at 278 nm plotted as a function of radial position. Data at intervals of 20 min are shown as dots for sedimentation at 40000 rpm. The monophasic sedimentation boundaries suggest that  $\Delta N60\text{-C/S-DUSP26}$  exists as a single species of a homogeneous oligomeric state. The middle panel shows the residuals between the fitted curve and raw data. The bottom panel shows the fitted distribution of the apparent sedimentation coefficient ( $s^*$ ) calculated for  $\Delta N60\text{-C/S-DUSP26}$  is 1.925 S (and  $s_{20,w} = 2.012$  S), which corresponds to an estimated molecular mass of  $\sim 18.1$  kDa, consistent with a monomer. A complete list of hydrodynamic parameters is given in Table 1. (B) Gel filtration analysis of purified  $\Delta N60\text{-C/S-DUSP26}$ . The Superdex 75 gel filtration column was calibrated using molecular mass markers, whose elution volumes and relative molecular masses are indicated by arrows.  $\Delta N60\text{-C/S-DUSP26}$  eluted after 91 mL, consistent with an  $\sim 20$  kDa monomeric species. The inset shows a calibration curve obtained by plotting elution volumes of molecular markers (in milliliters) vs known hydrodynamic radii ( $R_H$ ) (●). The hydrodynamic radius of  $\Delta N60\text{-C/S-DUSP26}$  estimated from this calibration (○) is  $\sim 21.0$  Å (Table 1).

a typical sedimentation profile of  $\Delta N60\text{-C/S-DUSP26}$  obtained in 20 mM HEPES (pH 7.0) and 150 mM sodium chloride at 4 °C.

In a concentration range from 5 to 100  $\mu\text{M}$ ,  $\Delta N60\text{-C/S-DUSP26}$  migrated as a homogeneous species characterized by a monophasic

**Table 2. Crystallographic Data Collection and Refinement Statistics**

Data Collection	
wavelength (Å)	0.9789
space group	P212121
unit cell dimensions (Å)	$a = 81.9, b = 82.3, c = 91.7$
angles (deg)	$\alpha = \beta = \gamma = 90$
resolution range (Å)	15–1.68
Wilson <i>B</i> factor (Å <sup>2</sup> )	20.0
total no. of observations	754413
no. of unique observations	69003
completeness (%)	96.3 (97.7)
<i>R</i> <sub>sym</sub> (%)	5.0 (55.3)
$\langle I \rangle / \langle \sigma(I) \rangle$	40.2 (3.8)
Refinement	
no. of reflections (10–1.68 Å)	64,739
<i>R</i> <sub>work</sub> / <i>R</i> <sub>free</sub> (%)	18.5/21.5
no. of copies in the asymmetric unit	4
no. of water molecules	491
<i>B</i> value of model (Å <sup>2</sup> )	
chain A	32.1
chain B	27.9
chain C	44.2
chain D	43.2
waters	41.1
rmsd from ideal	
bond lengths (Å)	0.006
bond angles (deg)	1.0
Ramachandran plot (%)	
core	95.5
allowed	4.5
generously allowed	0.0
disallowed	0.0

sedimentation boundary (Figure 2A). This is indicative of a single major (>94.7%) component in solution migrating with an apparent sedimentation coefficient (*s*<sup>\*</sup>) of 1.925 S (Table 1). Conversion of the distribution of the apparent sedimentation coefficient to molecular mass revealed a molecular mass of  $\sim 18.1 \pm 0.5$  kDa, which agrees well with that of a monomer of  $\Delta$ N60-C/S-DUSP26 (expected molecular mass of  $\sim 18.2$  kDa). Furthermore, the  $\Delta$ N60-C/S-DUSP26 frictional ratio (*f*/*f*<sub>0</sub>) of  $\sim 1.23$ , consistent with a globular protein with a hydrodynamic radius (*R*<sub>H</sub>) of  $\sim 22.7$  Å (Table 1). Essentially identical hydrodynamic parameters were measured for  $\Delta$ N60-DUSP26 (Table 1), confirming the active site mutation did not affect oligomerization. Finally, DUSP26-core was also monomeric in solution (sedimentation coefficient of  $\sim 1.811$  S) and had a globular shape (frictional ratio *f*/*f*<sub>0</sub> of  $\sim 1.20$ ) (Table 1), as expected for a minimal DSP core.

To validate the AUC data, we also investigated the hydrodynamic properties of  $\Delta$ N60-C/S-DUSP26 by gel filtration chromatography using a Superdex 75 column. At physiological salt concentrations, in a range of concentrations between 5 and 100  $\mu$ M,  $\Delta$ N60-C/S-DUSP26 migrated as a monodisperse major peak, eluting after  $\sim 91$  mL (Figure 2B). Molecular mass calibration standards confirmed this elution volume is consistent with an  $\sim 20$  kDa globular species with a hydrodynamic radius of  $\sim 21.0$  Å (Figure 2B and Table 1). Thus, in contrast to VH1<sup>13,14</sup> and DUSP27,<sup>36</sup>  $\Delta$ N60-C/S-DUSP26 adopts a monomeric conformation in solution.

**Atomic Structure of  $\Delta$ N60-DUSP26.** To shed light on the three-dimensional structure of DUSP26, we crystallized

$\Delta$ N60-DUSP26 and  $\Delta$ N60-C/S-DUSP26. As observed for VH1,<sup>13</sup> the active site mutant gave larger crystals that diffracted to 1.68 Å resolution using synchrotron radiation. The structure of  $\Delta$ N60-C/S-DUSP26 was determined by molecular replacement and refined to *R*<sub>work</sub> and *R*<sub>free</sub> values of 18.5 and 21.5%, respectively, using all reflections between 10 and 1.68 Å resolution (Table 2).  $\Delta$ N60-C/S-DUSP26 crystallized as a tetramer generated by two C-terminally swapped dimers (Figure 3A) rotated by 180° in the crystallographic asymmetric unit. Each  $\Delta$ N60-C/S-DUSP26 dimer is stabilized by helix  $\alpha$ 9, which is swapped between two protomers, thereby generating a compact structure 60 Å in length and  $\sim 45$  Å in width (Figure 3A). Because  $\Delta$ N60-C/S-DUSP26 has been proven to be monomeric in solution, at physiological ionic strengths and concentrations (between 5 and 100  $\mu$ M) (Figure 2), the domain-swapped dimer seen in the asymmetric unit likely reflects a crystallographic artifact caused by the high protein concentration achieved during crystallization and the presence of precipitant. The tertiary structure of  $\Delta$ N60-C/S-DUSP26 is illustrated in Figure 3B. The protein resembles a “lollipop”, built by a globular DSP domain  $\sim 40$  Å in diameter connected to a 35 Å long C-terminal helix ( $\alpha$ 9), nearly orthogonal to the phosphatase core. The dual-specificity phosphatase core (residues 61–187) (Figure 3B,C) consists of a central five-stranded  $\beta$ -sheet ( $\beta$ 1– $\beta$ 5) (highlighted in light blue in Figure 3C) sandwiched between two clusters of three  $\alpha$ -helices ( $\alpha$ 3– $\alpha$ 5 and  $\alpha$ 6– $\alpha$ 8) that surround the central core and make contacts with the solvent. The last DSP-core helix,  $\alpha$ 8, connects to the long helix  $\alpha$ 9 (residues 191–208), which is swapped between two subunits (Figure 3A–C). This helix is significantly longer than those in most DUSPs (20 residues vs 10–12 residues) and presents several conserved basic and hydrophobic residues.

**Architecture of the DUSP26 Active Site.** The 1.68 Å resolution structure of  $\Delta$ N60-C/S-DUSP26 provides a detailed view of the enzyme active site. The DUSP26 catalytic triad consists of Arg158, Asp120, and Cys152, which is replaced with a serine in our structure (Figure 4A). The conformation adopted by the PTP-binding loop (PTP-loop) in DUSP26 renders the active site pocket very shallow, almost imperceptible by scanning the enzyme surface (Figure 4B). Catalytic residue Cys152 (Ser152 in our structure) sits at the bottom of the active site, buried  $\sim 7$  Å below the enzyme surface, at a position that appears to have minimal solvent exchange. The DUSP26 catalytic triad, residues Arg158, Asp120, and Cys152, can be structurally superimposed on the catalytic triad of the prototypical VH1<sup>13</sup> (Figure 5A), as well as those of other VH1-related DUSPs such as VHZ<sup>37</sup> and DUSP27<sup>36</sup> (data not shown). However, the orientation of the PTP-loop of DUSP26 between residues 153 and 157 deviates significantly from that seen in VH1. In DUSP26 residues 153–157, main chain atoms are shifted  $\sim 3.5$  Å upward compared to those of VH1 and the carbonyl groups of Val154 and Gly155 point down inside the active site, as opposed to projecting outward as in VH1 (Figure 5A). This backbone conformation is made possible by the fact that position 155 of the PTP-loop of DUSP26 is occupied by a glycine (as opposed to alanine as in VH1<sup>13</sup>), which allows considerably greater main chain flexibility because of the small van der Waals radius of its single hydrogen atom side chain. Interestingly, the closed conformation of the PTP-loop of DUSP26 resembles the conformation visualized crystallographically in phosphatase MKP-4.<sup>38</sup> This protein also presents backbone carbonyl groups pointing into the active site and has minimal catalytic activity in the absence of substrate<sup>33</sup> (Figure 5B). Furthermore, the DUSP26 active site lacks a bulky phosphate

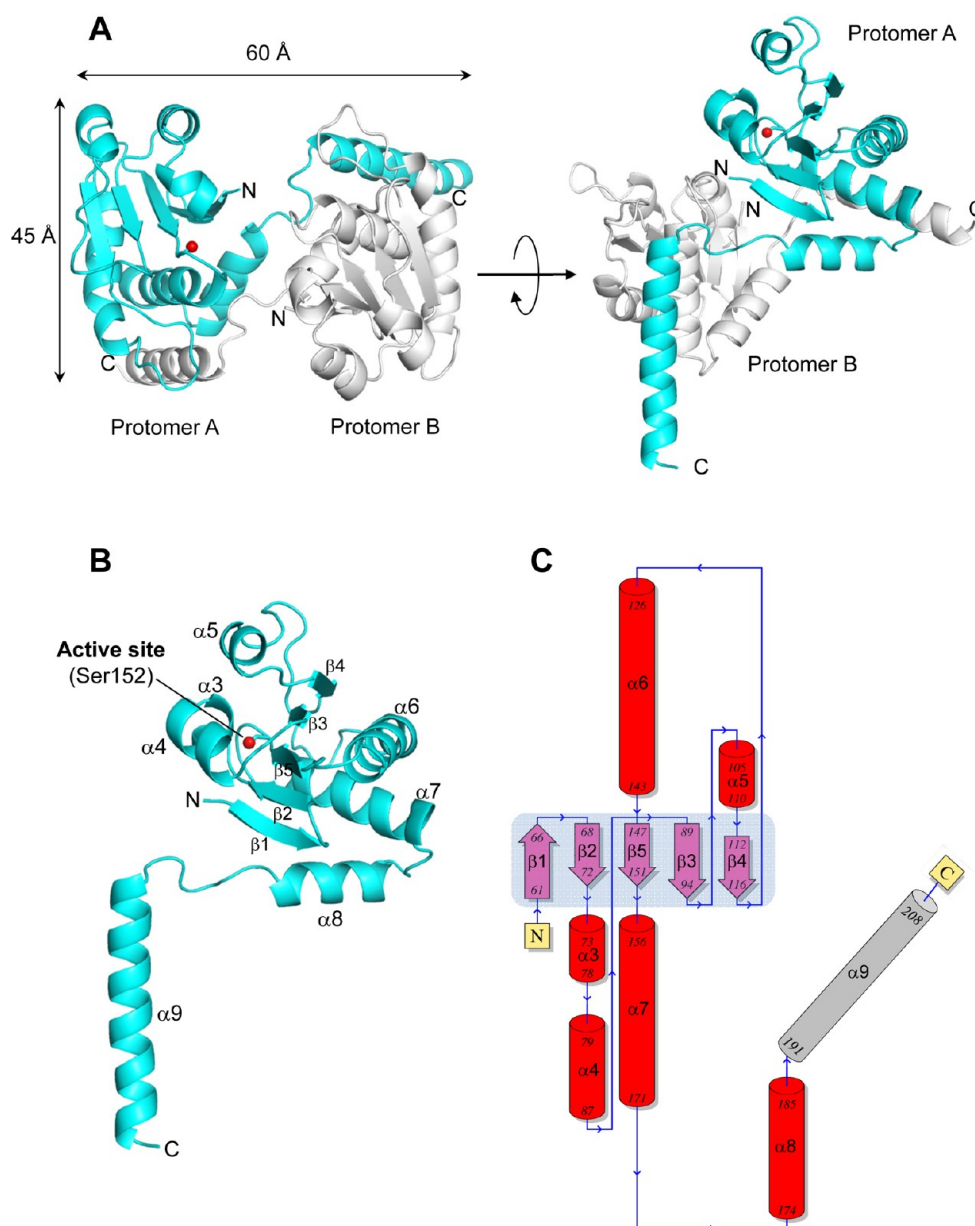


**Figure 3.** Atomic structure of  $\Delta\text{N60-C/S-DUSP26}$  at 1.68 Å resolution. (A) Ribbon diagram of the  $\Delta\text{N60-C/S-DUSP26}$  crystallographic dimer (side and top views) that is present in two copies in the asymmetric unit. Two protomers of a dimer (termed A and B) are colored cyan and gray, respectively. The position of the protomer A catalytic residue (Ser152) is shown as a red ball. (B) Ribbon diagram of protomer A showing all secondary structure elements. (C) Topological diagram of  $\Delta\text{N60-C/S-DUSP26}$  protomer A with  $\alpha$ -helices and  $\beta$ -strands forming the DSP-core colored red and purple, respectively, and domain-swapped helix  $\alpha 9$  colored gray. The central  $\beta$ -sheet formed by strands  $\beta 1$ – $\beta 5$  is shown with a light blue background. A complete list of crystallographic parameters is given in Table 2.

(or sulfate) ion (as seen in VH1<sup>13</sup> or DUSP27<sup>36</sup>) but is occupied by a water molecule (termed “active site water” or “ $W_{\text{AS}}$ ”) (Figure 4A), visible as an  $\sim 3.5\sigma$  peak in an  $F_o - F_c$  electron density difference map (Figure 5C). This active site water molecule is coordinated by backbone atoms of PTP-loop residues 153–158, and it makes close contacts (2.9–3.0 Å) with side chain atoms of Arg158, Ser152, and Asp120 (Figure 5C). Accordingly, the anisotropically refined  $B$  factor of  $W_{\text{AS}}$  varies between 22.5 and 31.0 Å<sup>2</sup> in the four protomers present in the asymmetric unit, which is significantly lower than the average  $B$  factor of protein (36.9 Å<sup>2</sup>) and solvent ( $\sim 41.1$  Å<sup>2</sup>) atoms (Table 2), underscoring slow solvent exchange.

**Evidence of a Closed Conformation of the C-Terminal Helix  $\alpha 9$ .** To investigate the degree of structural conservation,

we superimposed  $\Delta\text{N60-C/S-DUSP26}$  on the prototypical VH1, which we previously determined to 1.32 Å resolution<sup>13</sup> and whose crystallographic structure matches the conformation observed in solution.<sup>14</sup> Despite the low level of sequence identity ( $\sim 26\%$ ), the two phosphatases are structurally superimposable (rmsd of  $\sim 1.92$  Å), with 109 of 153 residues in DUSP26 topologically matched in VH1 (Figure 6A). While the DSP-core is remarkably conserved, the position of the C-terminal helix  $\alpha 9$  of DUSP26 is dramatically different from that of its counterpart in VH1, helix  $\alpha 6_{\text{VH1}}$  (highlighted in red in Figure 6A). In VH1, this helix adopts a closed conformation that packs against the DSP-core and engages in hydrophobic contacts with helix  $\alpha 4_{\text{VH1}}$  (continuous with the PTP-loop) (Figure 6A). In contrast, in our structure, helix  $\alpha 9$  swings 180°



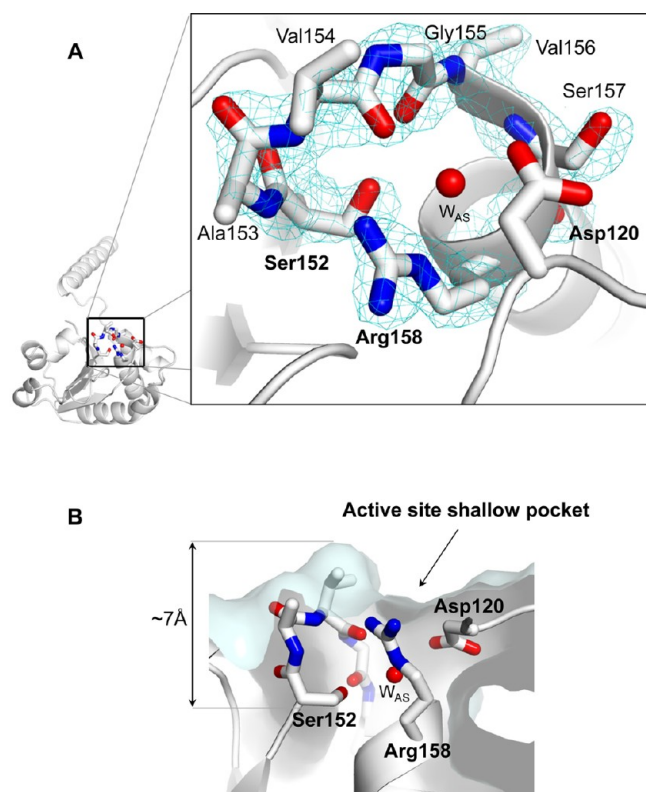


**Figure 4.** Architecture of the DUSP26 active site. (A) Magnified view of the  $\Delta$ N60-C/S-DUSP26 active site visualized at 1.68 Å resolution. The final  $2F_o - F_c$  electron density map contoured 1.5 $\sigma$  above background (cyan) is displayed around the refined model of the PTP-loop of  $\Delta$ N60-C/S-DUSP26 (shown as sticks). Residues forming the catalytic loops are labeled. (B) Cut-through view of the DUSP26 catalytic pocket revealing the location of Ser152, which is buried from the solvent  $\sim 7$  Å below the enzyme surface.

away from its DSP-core to make contacts with another subunit (“protomer B”), to which it is related by 2-fold noncrystallographic symmetry. Examination of the crystallographic domain-swapped interface (Figure 3A) (which, as previously demonstrated, represents a crystallographic artifact) reveals that helix  $\alpha 9$  of protomer B ( $\alpha 9_B$ ) (colored gray in Figure 6A) also packs against the DSP-core of protomer A, occupying the same position as helix  $\alpha 6_{VH1}$  in VH1. Thus, an intermolecular contact between the DSP-core of  $\Delta$ N60-C/S-DUSP26 protomer A and helix  $\alpha 9_B$  mimics in our crystal structure the closed conformation of helix  $\alpha 6_{VH1}$  generated intramolecularly in VH1. Helix  $\alpha 9_B$  also interacts with the general acid loop, mainly via electrostatic contacts between Asn191 (of protomer B) and Asp120 (of protomer A). This interaction does not perturb the conformation of the DUSP26 general acidic loop, which can be superimposed with its counterpart in VH1 (rmsd of  $\sim 1.1$  Å).

Next, we asked if the extended conformation of helix  $\alpha 9$  seen in the crystal is also populated in solution, or if this helix folds back onto its DSP-core to generate a globular structure similar to that of VH1.<sup>13</sup> To answer this question, we generated an atomic model of  $\Delta$ N60-C/S-DUSP26 with helix  $\alpha 9$  folded onto its DSP-core (closed- $\Delta$ N60-C/S-DUSP26) to mimic the position occupied by helix  $\alpha 9_B$  (or  $\alpha 6_{VH1}$ ) (Figure 6B). This model appears to be very plausible, as most of the hydrophobic residues mediating packing of helix  $\alpha 6_{VH1}$  to its DSP-core are also conserved in helix  $\alpha 9$  of DUSP26 (shown by arrows in Figure 6A). Accordingly, the hydrodynamic radius of

closed- $\Delta$ N60-C/S-DUSP26 calculated from atomic coordinates ( $\sim 24.3$  Å) is remarkably similar to  $\Delta$ N60-C/S-DUSP26’s  $R_H$  determined experimentally using velocity sedimentation analysis ( $\sim 22.7$  Å) and gel filtration chromatography ( $\sim 21.0$  Å) and strikingly smaller than the  $R_H$  measured from the crystallographic coordinates of  $\Delta$ N60-C/S-DUSP26 ( $\sim 37.9$  Å) (Figure 6B and Table 1). Thus,  $\Delta$ N60-C/S-DUSP26 exists in solution in a conformation more globular than in crystal, likely because of the closed conformation of helix  $\alpha 9$ .

## DISCUSSION

More than 50% of all human cancers have mutations or deletions in the p53 gene.<sup>24</sup> In neuroblastoma, an aggressive pediatric malignancy, p53 levels are mostly wild-type levels but the protein is poorly active because of hypo-phosphorylation of its TAD, which is partially structured in solution.<sup>39</sup> In the classical model of p53 activation, exposure to DNA-damaging agents and cytotoxic stress result in phosphorylation at several Ser and Thr residues in p53-TAD, which is important for p53 stabilization, DNA binding, and transcriptional activity.<sup>40–42</sup> In particular, phosphorylation of Ser20 creates a phospho-SDLxxLL docking motif critical to the stabilization of the binding of the transcriptional coactivator p300.<sup>43–45</sup> Misregulation of p53 stabilization by dephosphorylation of its TAD is linked to chemoresistance in neuroblastoma and other cancers.<sup>46,47</sup> Hypophosphorylated p53 is in fact unstable and has reduced tumor suppressor function,<sup>40</sup> which contributes to chemoresistance, tumor metastasis, and poor patient survival.<sup>48–50</sup> Shang et al. recently demonstrated that DUSP26 is highly overexpressed in neuroblastoma, where it represses p53 oncosuppressor function by specifically dephosphorylating pSer20 and pSer37.<sup>21</sup> Furthermore, a high level of DUSP26 promotes resistance of human neuroblastoma to doxorubicin, a drug commonly used in cancer chemotherapy. As a corollary, inhibition of DUSP26 is a potential target for enhancing p53-mediated response, which could be useful for the treatment of neuroblastomas insensitive to chemotherapy and increase the likelihood of the success of treatment. The 1.68 Å crystal structure of  $\Delta$ N60-C/S-DUSP26 presented here provides the first atomic insight into this disease-associated phosphatase.

**DUSP26 Is a Monomeric Phosphatase.** Dimerization is emerging as an important structural determinant for small dual-specificity phosphatases, previously assumed to be monomeric. In at least three cases, dimerization has been shown to modulate phosphatase catalytic activity. Liu et al. demonstrated that laforin dimerization is essential for phospho-glycogen recognition and catalytic activity.<sup>51</sup> Likewise, dimerization of myotubularin (MTM)-related protein 2 (MTMR2) via a C-terminal coiled coil was found to be essential for membrane association and phosphoinositide dephosphorylation.<sup>52</sup> Finally, we recently demonstrated that VH1 dimeric structure is essential for recognition and dephosphorylation of activated STAT1.<sup>13,14</sup> The crystal structure of DUSP27 was also recently reported,<sup>36</sup> and as in VH1, this phosphatase also dimerizes via an N-terminal domain-swapped  $\alpha$ -helix. In contrast, in this paper we provide compelling evidence that  $\Delta$ N60-C/S-DUSP26 adopts a monomeric conformation in solution, in a range of concentrations between 5 and 100  $\mu$ M, likely close to the physiological concentration of DUSP26 in brain cells. Using sedimentation velocity analysis and gel filtration chromatography, we determined that  $\Delta$ N60-C/S-DUSP26 exists in solution as a globular species with a hydrodynamic radius ( $R_H$ ) of  $\sim 22.7/21.0$  Å

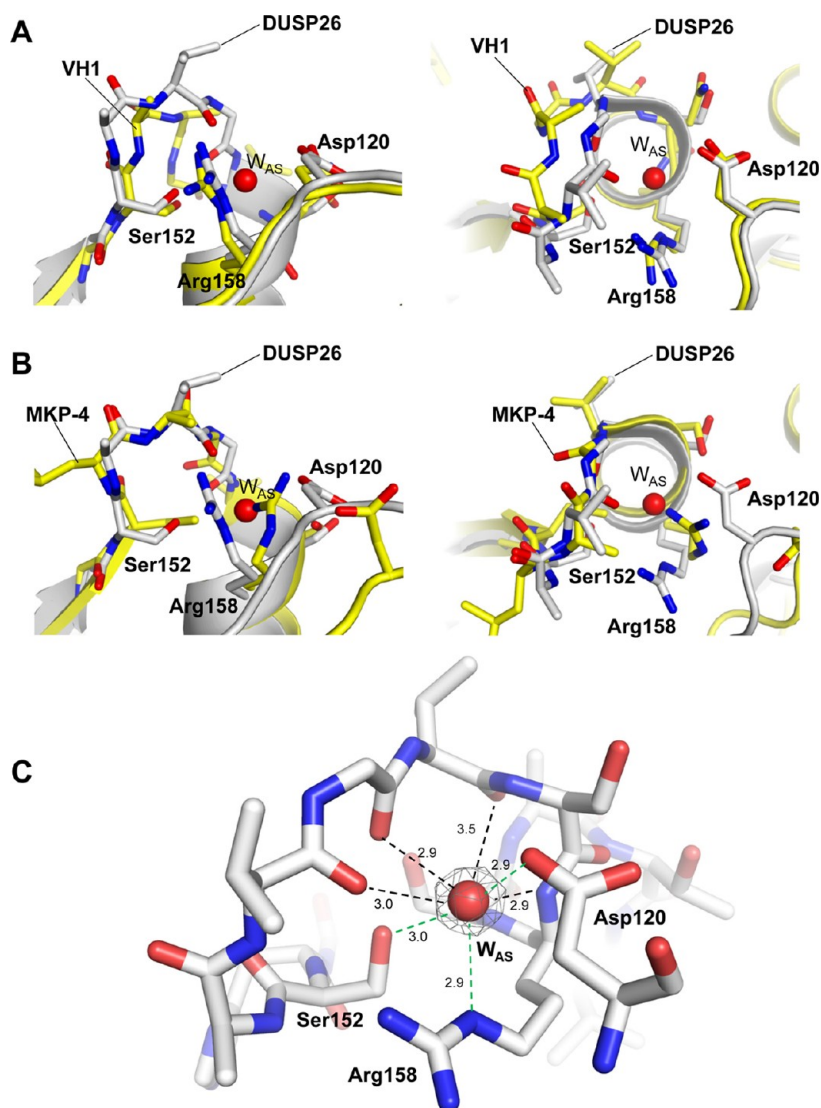


**Figure 5.** Conformation of the PTP-loop of DUSP26. Superimposition of the PTP-loop of  $\Delta$ N60-C/S-DUSP26 with VH1 (PDB entry 3CM3) (A) and MKP-4 (PDB entry 3LJ8) (B), in side (left) and top views (right). In all panels, DUSP26 is colored gray while VH1 and MKP-4 are colored yellow. For the sake of clarity, only the DUSP26 catalytic triad and  $W_{AS}$  have been labeled (and the phosphate ion trapped in the VH1 active site has been omitted). (C) Snapshot of  $\Delta$ N60-C/S-DUSP26  $W_{AS}$  (red sphere) trapped inside the PTP-loop (shown as sticks). An  $F_o - F_c$  electron density map (colored gray) contoured  $3.5\sigma$  above background is overlaid on  $W_{AS}$ . The density was calculated after  $W_{AS}$  had been omitted from the refined model. Distances between  $W_{AS}$  and PTP-loop main and side chain atoms are indicated by black and green dashed lines, respectively.

(Table 1). This conformation is different from the crystallographic structure, which is elongated because of the extended conformation adopted by helix  $\alpha 9$ . Structural comparison of  $\Delta$ N60-C/S-DUSP26 with VH1 suggested that the extended conformation of helix  $\alpha 9$  seen in the crystal is stabilized by a crystallographic contact with another protomer (protomer B), which packs its helix  $\alpha 9_B$  against the DSP-core, mimicking the closed conformation seen in VH1 (Figure 6A). Although this crystallographic packing results in an artificial dimeric structure (Figure 3A) that is not observed in solution, the ability of helix  $\alpha 9$  to swing by  $>180^\circ$  around its DSP-core reflects the potential flexibility of this secondary structure element. Intriguingly, the extended conformation of helix  $\alpha 9$  projects five basic residues to the solvent (Arg192, -196, -203, -204, and -206), all clustered on one side of the helix (Figure 7). These residues generate a continuous basic surface that, together with four arginines from helix  $\alpha 4$  (Figure 3B,C) and a few residues from the DSP-core, accounts for 11 arginines, all facing the solvent (Figure 7).

We speculate this continuous basic surface clustered on one side of the enzyme could provide an attachment point for highly acidic substrates, such as the phosphorylated p53-TAD, and promote the recruitment of substrate to DUSP26. Because the closed conformation of helix  $\alpha 9$  is predicted to pack against helix  $\alpha 7$ , which is directly continuous with the PTP-loop (Figure 6A), this interaction may trigger a conformational change in the PTP-loop that mediates its activation. The PTP-loop of DUSP26 observed crystallographically is in fact closed and tightly coordinated to a water molecule (Figure 5C). In analogy to phosphatase MKP-4,<sup>38</sup> which presents a closed conformation of the PTP-loop and has minimal catalytic activity in the absence of substrate,<sup>53</sup> substrate binding to DUSP26 may trigger a conformational change that opens the PTP-loop, thereby marking the transition from an inactive to an active conformation of the phosphatase. The suggested mechanism is distinct from that proposed for VH1 and laforin, in which dimerization is thought to be essential for catalytic



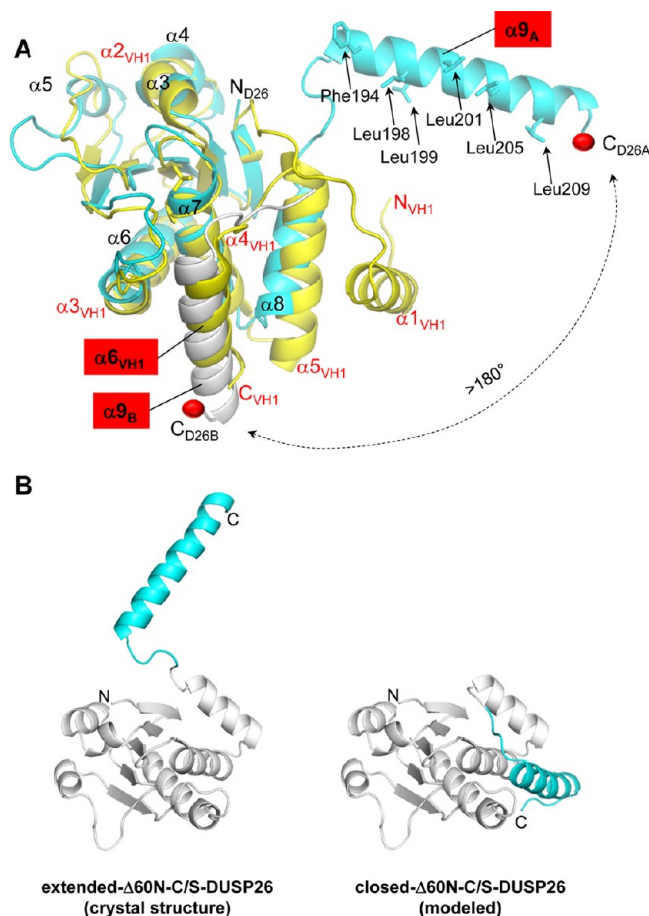


**Figure 6.** Flexibility of the C-terminal helix  $\alpha 9$  of DUSP26. (A) Superimposition of  $\Delta N60$ -C/S-DUSP26 and VH1 (colored cyan and yellow, respectively). For the sake of clarity, only  $\alpha$ -helices are labeled; helix  $\alpha 9$  and its counterpart in VH1, helix  $\alpha 6_{VH1}$ , are highlighted in red. Hydrophobic residues protruding on the surface of helix  $\alpha 9$  are shown as sticks and their positions indicated by arrows. Helix  $\alpha 9$  of protomer B ( $\alpha 9_B$ ) is shown as a gray ribbon. A red ball indicates the position of the  $\alpha 9_A$  and  $\alpha 9_B$  C-termini of DUSP26; a dashed arrow illustrates the putative trajectory of the conformational change helix  $\alpha 9$  would undergo from the position observed crystallographically to that adopted by helix  $\alpha 6_{VH1}$  in VH1 (or helix  $\alpha 9_B$  in protomer B). (B) Ribbon diagram of the  $\Delta N60$ -C/S-DUSP26 protomer observed crystallographically, with helix  $\alpha 9$  in an extended conformation (extended- $\Delta N60$ -C/S-DUSP26), and of a model of  $\Delta N60$ -C/S-DUSP26 with helix  $\alpha 9$  packed against the DSP-core like in VH1 (closed- $\Delta N60$ -C/S-DUSP26). In both diagrams, the DSP-core is colored gray and helix  $\alpha 9$  cyan.

activity, by generating a binding surface complementary to the phospho-substrate (phosphorylated STAT1 for VH1<sup>13,14</sup> and phospho-glycogen<sup>12</sup> for laforin).

**Concluding Remarks.** Several debilitating human diseases such as cancer, diabetes, inflammation, and Alzheimer's disease are intimately linked to DUSPs. Inhibiting DUSPs is a potential therapeutic strategy of great interest in pharmacology.<sup>54,55</sup> Unlike kinases, for which the molecular determinants for substrate specificity are well understood,<sup>56</sup> it is unclear how DUSPs selectively recognize their substrates. In this paper, we have described the structural organization of human DUSP26 and characterized its conformational stability and oligomeric state in solution. This work is a step forward toward characterizing DUSP26 composition and biologically active conformation. DUSP26 is indeed a powerful and novel

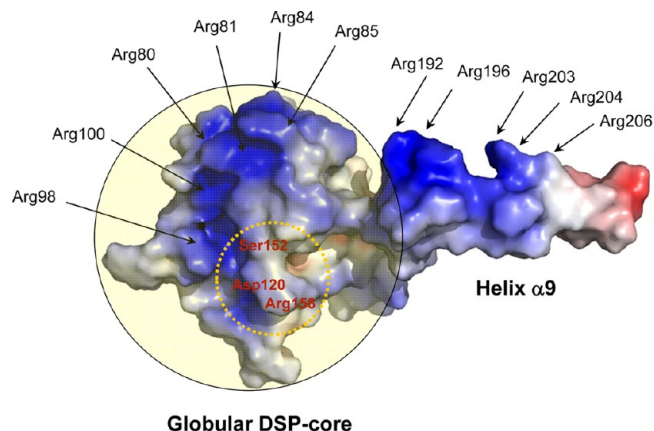


**Figure 7.** Electrostatic surface potential of  $\Delta N60$ -C/S-DUSP26. Arginines exposed on the surface of  $\Delta N60$ -C/S-DUSP26 (mainly helices  $\alpha 9$  and  $\alpha 4$ ) are shown with arrows. The DSP-core is overlaid with a semitransparent yellow circle. Active site residues are circled by a dashed yellow line.

therapeutic target for the treatment of aggressive pediatric malignancy, and its inhibition may be of great usefulness for increasing neuroblastoma chemosensitivity.

## AUTHOR INFORMATION

### Corresponding Author

\*Department of Biochemistry and Molecular Biology, Thomas Jefferson University, 233 S. 10th St., Philadelphia, PA 19107. E-mail: gino.cingolani@jefferson.edu. Telephone: (215) 503-4573. Fax: (215) 923-2117.

### Funding

This work was supported in part by National Institutes of Health Grant GM074846-01A1.

### Notes

The authors declare no competing financial interest.

## ACKNOWLEDGMENTS

We are thankful to Vivian Stojanoff, Marc Allaire, and the scientific staff at National Synchrotron Light Source beamlines X6A and X29 for assistance and help in data collection. Research in this publication includes work conducted at the Kimmel Cancer Center X-ray Crystallography and Molecular Interaction Facility, which is supported in part by National Cancer Institute Cancer Center Support Grant P30 CA56036.

## ABBREVIATIONS

DUSP26, dual-specificity phosphatase 26; DSP, dual-specificity phosphatase; PTP, protein tyrosine phosphatase; TAD, trans-activation domain; CD, circular dichroism; AUC, analytical ultracentrifugation;  $R_H$ , hydrodynamic radius;  $appT_m$ , apparent melting temperature;  $W_{AS}$ , active site water.

## REFERENCES

- (1) Denu, J. M., Stuckey, J. A., Saper, M. A., and Dixon, J. E. (1996) Form and function in protein dephosphorylation. *Cell* 87, 361–364.
- (2) Zhang, Z. Y. (2002) Protein tyrosine phosphatases: Structure and function, substrate specificity, and inhibitor development. *Annu. Rev. Pharmacol. Toxicol.* 42, 209–234.
- (3) Alonso, A., Sasin, J., Bottini, N., Friedberg, I., Osterman, A., Godzik, A., Hunter, T., Dixon, J., and Mustelin, T. (2004) Protein tyrosine phosphatases in the human genome. *Cell* 117, 699–711.

- (4) Ducruet, A. P., Vogt, A., Wipf, P., and Lazo, J. S. (2005) Dual specificity protein phosphatases: Therapeutic targets for cancer and Alzheimer's disease. *Annu. Rev. Pharmacol. Toxicol.* 45, 725–750.
- (5) Patterson, K. I., Brummer, T., O'Brien, P. M., and Daly, R. J. (2009) Dual-specificity phosphatases: Critical regulators with diverse cellular targets. *Biochem. J.* 418, 475–489.
- (6) Guan, K. L., Broyles, S. S., and Dixon, J. E. (1991) A Tyr/Ser protein phosphatase encoded by vaccinia virus. *Nature* 350, 359–362.
- (7) Phan, J., Tropea, J. E., and Waugh, D. S. (2007) Structure-assisted discovery of Variola major H1 phosphatase inhibitors. *Acta Crystallogr. D* 63, 698–704.
- (8) Jackson, M. D., and Denu, J. M. (2001) Molecular reactions of protein phosphatases: Insights from structure and chemistry. *Chem. Rev.* 101, 2313–2340.
- (9) Alonso, A., Burkhalter, S., Sasin, J., Tautz, L., Bogetz, J., Huynh, H., Bremer, M. C., Holsinger, L. J., Godzik, A., and Mustelin, T. (2004) The minimal essential core of a cysteine-based protein-tyrosine phosphatase revealed by a novel 16-kDa VH1-like phosphatase, VHZ. *J. Biol. Chem.* 279, 35768–35774.
- (10) Maehama, T., Taylor, G. S., and Dixon, J. E. (2001) PTEN and myotubularin: Novel phosphoinositide phosphatases. *Annu. Rev. Biochem.* 70, 247–279.
- (11) Deshpande, T., Takagi, T., Hao, L., Buratowski, S., and Charbonneau, H. (1999) Human PIR1 of the protein-tyrosine phosphatase superfamily has RNA 5'-triphosphatase and diphosphatase activities. *J. Biol. Chem.* 274, 16590–16594.
- (12) Tagliabracci, V. S., Turnbull, J., Wang, W., Girard, J. M., Zhao, X., Skurat, A. V., Delgado-Escueta, A. V., Minassian, B. A., Depaoli-Roach, A. A., and Roach, P. J. (2007) Laforin is a glycogen phosphatase, deficiency of which leads to elevated phosphorylation of glycogen in vivo. *Proc. Natl. Acad. Sci. U.S.A.* 104, 19262–19266.
- (13) Koksai, A. C., Nardozi, J. D., and Cingolani, G. (2009) Dimeric quaternary structure of the prototypical dual specificity phosphatase VH1. *J. Biol. Chem.* 284, 10129–10137.
- (14) Koksai, A. C., and Cingolani, G. (2011) Dimerization of Vaccinia Virus VH1 Is Essential for Dephosphorylation of STAT1 at Tyrosine 701. *J. Biol. Chem.* 286, 14373–14382.
- (15) Vasudevan, S. A., Skoko, J., Wang, K., Burlingame, S. M., Patel, P. N., Lazo, J. S., Nuchtern, J. G., and Yang, J. (2005) MKP-8, a novel MAPK phosphatase that inhibits p38 kinase. *Biochem. Biophys. Res. Commun.* 330, 511–518.
- (16) Takagaki, K., Shima, H., Tanuma, N., Nomura, M., Satoh, T., Watanabe, M., and Kikuchi, K. (2007) Characterization of a novel low-molecular-mass dual specificity phosphatase-4 (LDP-4) expressed in brain. *Mol. Cell. Biochem.* 296, 177–184.
- (17) Hu, Y., and Mivechi, N. F. (2006) Association and regulation of heat shock transcription factor 4b with both extracellular signal-regulated kinase mitogen-activated protein kinase and dual-specificity tyrosine phosphatase DUSP26. *Mol. Cell. Biol.* 26, 3282–3294.
- (18) Wang, J. Y., Lin, C. H., Yang, C. H., Tan, T. H., and Chen, Y. R. (2006) Biochemical and biological characterization of a neuro-endocrine-associated phosphatase. *J. Neurochem.* 98, 89–101.
- (19) Yu, W., Imoto, I., Inoue, J., Onda, M., Emi, M., and Inazawa, J. (2007) A novel amplification target, DUSP26, promotes anaplastic thyroid cancer cell growth by inhibiting p38 MAPK activity. *Oncogene* 26, 1178–1187.
- (20) Tanuma, N., Nomura, M., Ikeda, M., Kasugai, I., Tsubaki, Y., Takagaki, K., Kawamura, T., Yamashita, Y., Sato, I., Sato, M., Katakura, R., Kikuchi, K., and Shima, H. (2009) Protein phosphatase Dusp26 associates with KIF3 motor and promotes N-cadherin-mediated cell-cell adhesion. *Oncogene* 28, 752–761.
- (21) Shang, X., Vasudevan, S. A., Yu, Y., Ge, N., Ludwig, A. D., Wesson, C. L., Wang, K., Burlingame, S. M., Zhao, Y. J., Rao, P. H., Lu, X., Russell, H. V., Okcu, M. F., Hicks, M. J., Shohet, J. M., Donehower, L. A., Nuchtern, J. G., and Yang, J. (2010) Dual-specificity phosphatase 26 is a novel p53 phosphatase and inhibits p53 tumor suppressor functions in human neuroblastoma. *Oncogene* 29, 4938–4946.
- (22) Cabre, F., Canela, E. I., and Canela, M. A. (1989) Accuracy and precision in the determination of Stokes radii and molecular masses of proteins by gel filtration chromatography. *J. Chromatogr.* 472, 347–356.
- (23) Lee, W. L., Ostap, E. M., Zot, H. G., and Pollard, T. D. (1999) Organization and ligand binding properties of the tail of Acanthamoeba myosin-1A. Identification of an actin-binding site in the basic (tail homology-1) domain. *J. Biol. Chem.* 274, 35159–35171.
- (24) Bhardwaj, A., Olia, A. S., Walker-Kopp, N., and Cingolani, G. (2007) Domain organization and polarity of tail needle GP26 in the portal vertex structure of bacteriophage P22. *J. Mol. Biol.* 371, 374–387.
- (25) Otwinowski, Z., and Minor, W. (1997) Processing of X-ray Diffraction Data Collected in Oscillation Mode. *Methods Enzymol.* 276, 307–326.
- (26) McCoy, A. J., Grosse-Kunstleve, R. W., Adams, P. D., Winn, M. D., Storoni, L. C., and Read, R. J. (2007) Phaser crystallographic software. *J. Appl. Crystallogr.* 40, 658–674.
- (27) Emsley, P., and Cowtan, K. (2004) Coot: Model-building tools for molecular graphics. *Acta Crystallogr. D* 60, 2126–2132.
- (28) Adams, P. D., Afonine, P. V., Bunkoczi, G., Chen, V. B., Davis, I. W., Echols, N., Headd, J. J., Hung, L. W., Kapral, G. J., Grosse-Kunstleve, R. W., McCoy, A. J., Moriarty, N. W., Oeffner, R., Read, R. J., Richardson, D. C., Richardson, J. S., Terwilliger, T. C., and Zwart, P. H. (2004) PHENIX: A comprehensive Python-based system for macromolecular structure solution. *Acta Crystallogr. D* 66, 213–221.
- (29) Murshudov, G. N., Vagin, A. A., and Dodson, E. J. (1997) Refinement of macromolecular structures by the maximum-likelihood method. *Acta Crystallogr. D* 53, 240–255.
- (30) Collaborative Computational Project Number 4 (1994) The CCP4 suite: Programs for protein crystallography. *Acta Crystallogr. D* 50, 760–763.
- (31) DeLano, W. L. (2002) *The PyMOL Molecular Graphics System*, DeLano Scientific, San Carlos, CA.
- (32) Dolinsky, T. J., Nielsen, J. E., McCammon, J. A., and Baker, N. A. (2004) PDB2PQR: An automated pipeline for the setup of Poisson-Boltzmann electrostatics calculations. *Nucleic Acids Res.* 32, W665–W667.
- (33) Laskowski, R. A. (2009) PDBsum new things. *Nucleic Acids Res.* 37, D355–D359.
- (34) Krissinel, E., and Henrick, K. (2007) Inference of macromolecular assemblies from crystalline state. *J. Mol. Biol.* 372, 774–797.
- (35) Ortega, A., Amoros, D., and Garcia de la Torre, J. (2011) Prediction of hydrodynamic and other solution properties of rigid proteins from atomic- and residue-level models. *Biophys. J.* 101, 892–898.
- (36) Lountos, G. T., Tropea, J. E., and Waugh, D. S. (2011) Structure of human dual-specificity phosphatase 27 at 2.38 Å resolution. *Acta Crystallogr. D* 67, 471–479.
- (37) Yuvaniyama, J., Denu, J. M., Dixon, J. E., and Saper, M. A. (1996) Crystal structure of the dual specificity protein phosphatase VHR. *Science* 272, 1328–1331.
- (38) Jeong, D. G., Yoon, T. S., Jung, S. K., Park, B. C., Park, H., Ryu, S. E., and Kim, S. J. (2011) Exploring binding sites other than the catalytic core in the crystal structure of the catalytic domain of MKP-4. *Acta Crystallogr. D* 67, 25–31.
- (39) Lee, C. W., Martinez-Yamout, M. A., Dyson, H. J., and Wright, P. E. (2010) Structure of the p53 transactivation domain in complex with the nuclear receptor coactivator binding domain of CREB binding protein. *Biochemistry* 49, 9964–9971.
- (40) Kruse, J. P., and Gu, W. (2009) Modes of p53 regulation. *Cell* 137, 609–622.
- (41) Levine, A. J. (1997) p53, the cellular gatekeeper for growth and division. *Cell* 88, 323–331.
- (42) Meek, D. W. (2009) Tumour suppression by p53: A role for the DNA damage response? *Nat. Rev. Cancer* 9, 714–723.
- (43) Dornan, D., and Hupp, T. R. (2001) Inhibition of p53-dependent transcription by BOX-I phospho-peptide mimetics that bind to p300. *EMBO Rep.* 2, 139–144.

- (44) Dornan, D., Shimizu, H., Perkins, N. D., and Hupp, T. R. (2003) DNA-dependent acetylation of p53 by the transcription coactivator p300. *J. Biol. Chem.* 278, 13431–13441.
- (45) Dornan, D., Shimizu, H., Burch, L., Smith, A. J., and Hupp, T. R. (2003) The proline repeat domain of p53 binds directly to the transcriptional coactivator p300 and allosterically controls DNA-dependent acetylation of p53. *Mol. Cell. Biol.* 23, 8846–8861.
- (46) Tweddle, D. A., Malcolm, A. J., Bown, N., Pearson, A. D., and Lunec, J. (2001) Evidence for the development of p53 mutations after cytotoxic therapy in a neuroblastoma cell line. *Cancer Res.* 61, 8–13.
- (47) Maclaine, N. J., and Hupp, T. R. (2009) The regulation of p53 by phosphorylation: A model for how distinct signals integrate into the p53 pathway. *Aging* 1, 490–502.
- (48) Moll, U. M., Ostermeyer, A. G., Ahomadegbe, J. C., Mathieu, M. C., and Riou, G. (1995) p53 mediated tumor cell response to chemotherapeutic DNA damage: A preliminary study in matched pairs of breast cancer biopsies. *Hum. Pathol.* 26, 1293–1301.
- (49) Moll, U. M., LaQuaglia, M., Benard, J., and Riou, G. (1995) Wild-type p53 protein undergoes cytoplasmic sequestration in undifferentiated neuroblastomas but not in differentiated tumors. *Proc. Natl. Acad. Sci. U.S.A.* 92, 4407–4411.
- (50) Vousden, K. H., and Lu, X. (2002) Live or let die: The cell's response to p53. *Nat. Rev. Cancer* 2, 594–604.
- (51) Liu, Y., Wang, Y., Wu, C., Liu, Y., and Zheng, P. (2006) Dimerization of laforin is required for its optimal phosphatase activity, regulation of GSK3 $\beta$  phosphorylation, and Wnt signaling. *J. Biol. Chem.* 281, 34768–34774.
- (52) Berger, P., Schaffitzel, C., Berger, I., Ban, N., and Suter, U. (2003) Membrane association of myotubularin-related protein 2 is mediated by a pleckstrin homology-GRAM domain and a coiled-coil dimerization module. *Proc. Natl. Acad. Sci. U.S.A.* 100, 12177–12182.
- (53) Camps, M., Nichols, A., Gillieron, C., Antonsson, B., Muda, M., Chabert, C., Boschert, U., and Arkinstall, S. (1998) Catalytic activation of the phosphatase MKP-3 by ERK2 mitogen-activated protein kinase. *Science* 280, 1262–1265.
- (54) Lazo, J. S., and Wipf, P. (2009) Phosphatases as targets for cancer treatment. *Curr. Opin. Invest. Drugs* 10, 1297–1304.
- (55) Bakan, A., Lazo, J. S., Wipf, P., Brummond, K. M., and Bahar, I. (2008) Toward a molecular understanding of the interaction of dual specificity phosphatases with substrates: Insights from structure-based modeling and high throughput screening. *Curr. Med. Chem.* 15, 2536–2544.
- (56) Ubersax, J. A., and Ferrell, J. E., Jr. (2007) Mechanisms of specificity in protein phosphorylation. *Nat. Rev. Mol. Cell Biol.* 8, 530–541.